Nanoscale

Accepted Manuscript

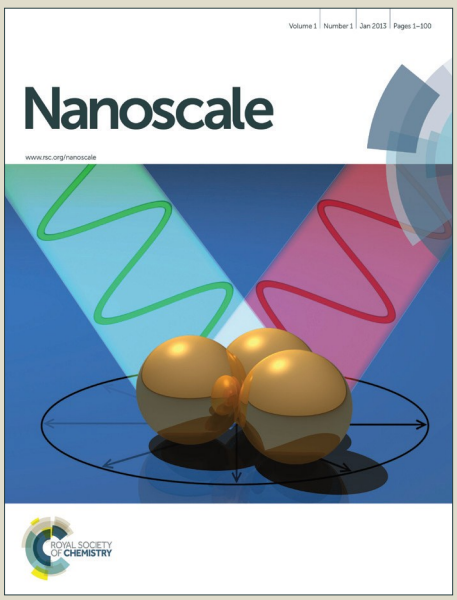

ROYAL SOCIETY OF CHEMISTRY

www.rsc.org/nanoscale

Journal Name

RSCPublishing

ARTICLE

Charge Transfer vs. Dimensionality: What affects the Transport Properties of Ferecrystals?

Cite this: DOI: 10.1039/x0xx00000x

Matti B. Alemayehu,[a*] Kim Ta,[a] Matthias Falmbigl[a] and David C. Johnson[a]

Received ooth January 2012,
Accepted ooth January 2012

DOI: 10.1039/x0xx00000x

www.rsc.org/

A series of $([SnSe]_{1+\delta})_m(NbSe_2)_2$ compounds with two layers of $NbSe_2$ separated by *m* bilayers of SnSe, where $1 \leq m \leq 20$, were prepared from modulated precursors by systematically changing the number of SnSe layers in the repeating unit. A change in the *c*-lattice parameter of 0.579(3) nm per SnSe bilayer was observed. The thickness of the $NbSe_2$ layer was determined to be 1.281(4) nm: twice the value of a single $NbSe_2$ layer. HAADF-STEM images revealed the presence of extensive rotational disorder and the lack of any epitaxial relationship among the constituent layers. Two different coordination environments for the Nb in $NbSe_2$ (trigonal prismatic and octahedral) were observed. The electrical resistivity increases and the carrier concentration decreases in the $([SnSe]_{1+\delta})_m(NbSe_2)_2$ compounds with increasing number of SnSe bilayers. The temperature dependence of the resistivity suggests localization of carriers for higher *m* values. The decline in carrier concentration as a function of *m* implies the presence of charge transfer from SnSe to $NbSe_2$. The transport properties of $([SnSe]_{1+\delta})_m(NbSe_2)_2$ compounds and the previously reported $([SnSe]_{1+\delta})_m(NbSe_2)_1$ compounds both have unusually temperature independent resistivity compared to bulk $NbSe_2$. Compounds with similar *m*/*n* ratios exhibit similar transport properties. Consequently, the dominant effect on the transport properties of $([SnSe]_{1+\delta})_m(NbSe_2)_2$ is charge transfer and there are only subtle differences between a monolayer and a bilayer of $NbSe_2$.

Introduction

The first isolation of graphene in 2004[1] has led to a resurgence of interest in the study of other quasi two-dimensional layered materials[2,3] including the transition metal dichalcogenides (TMDs).[4–6] In particular, it has been shown that these compounds can form the basis of truly two-dimensional atomic crystals with remarkably diverse electronic properties and very high specific surface areas, making them suited for applications ranging from electronic devices to energy storage.[7,8] Understanding the effect of interlayer interaction and dimensionality on fundamental electrical properties in these layered materials at the nanoscale level will be crucial for electronic and electrochemical device applications.[8,9]

There are now many reports of abrupt differences in properties between monolayers and thicker stacks of layers, starting with the initial reports on graphene.[1,2,5] A prominent example is MoS_2, where a transition from an indirect to a direct band gap was predicted when thinning the bulk down to a monolayer.[2,10,11] The change in dimensionality from three to two has been shown to lead to changes in interlayer coupling, degree of quantum confinement and electronic structures.[12] Monolayers of metallic TMDs have been reported to have dramatically different properties than their bulk counter parts, e.g. NbX_2 and TaX_2, which show a CDW and a superconducting transition in bulk, have been reported to exhibit semiconducting properties as nanosheets.[13,14] There are also reports where ultra-thin films maintain bulk properties, for example the charge density wave (CDW) transition is still observed in nanosheets of metallic VSe_2.[15] A challenge in these investigations is determining the structure of the single layer, which is assumed to be bulk-like, and understanding the interaction between the monolayers and the substrate.[16]

We have approached these challenges by preparing ordered composite structures consisting of a rock salt structured constituent and a transition metal dichalcogenide.[17,18] Our synthesis approach produces extremely ordered, crystallographically aligned materials and the ability to independently vary the thickness of either constituent.[19,20] The 00*l* diffraction pattern of the composite alloys permits the position of the atomic planes to be determined.[21] The ability to vary *m* and *n* permits a systematic investigation of properties as a function of structure.[22] In the intergrowth compounds $([SnSe]_{1.16})_m(NbSe_2)_1$, we recently reported that increasing the thickness of the semiconducting SnSe constituent electronically isolates the $NbSe_2$ and enhances the two-dimensionality of the $NbSe_2$ monolayers.[23] The change in properties with *m*, however also is a function of charge transfer from the SnSe layer to the $NbSe_2$. Here, we report the synthesis and structure of a series of

$([SnSe]_{1+\delta})_m(NbSe_2)_2$ or (m,2) compounds, where two layers of $NbSe_2$ are interleaved with SnSe of growing thickness, to probe the effect of doubling the thickness of $NbSe_2$ on electrical properties. Comparing the structural and transport properties to $([SnSe]_{1+\delta})_m(NbSe_2)_1$ allows us to separate the influence of dimensionality from charge transfer between the layers. The results show that charge transfer dictates the transport properties of these compounds, with carrier concentration tracking with the m/n ratio. The electrical conductivity of the (m,2) compounds is remarkably independent of temperature compared to the bulk $NbSe_2$ and Hall measurements imply a higher mobility than found in the bulk $NbSe_2$. Moreover, a thickness limitation of the charge transfer in the SnSe is observed for values higher than 4.5 nm.

Experimental

The compounds $([SnSe]_{1+\delta})_m(NbSe_2)_2$, where $1 \leq m \leq 20$ were synthesized via the modulated elemental reactants (MER) technique as described in detail elsewhere,[24] using a custom-built vacuum chamber evacuated to a base pressure of 1×10^{-8} Torr. The elemental sources, Sn (99.999% purity), Nb (99.999% purity) and Se (99.999% purity), were purchased from Alfa Aesar. The precursors were evaporated onto a (100) oriented silicon wafers with the use of Thermionics 3kW *e*-beam guns. Sn, Nb and Se were evaporated at the rate of 0.04 nm/s, 0.02 nm/s and Se 0.05 nm/s respectively. A sequential LabView program was used to position the wafers on top of each elemental source. A pneumatic shutter was used to control the thickness of the materials deposited onto the silicon wafer, until a film thickness of ~ 50 nm was reached. A precursor with the same sequence and stoichiometry as the targeted compound is designed. Atomic composition and thickness ratio calibrations for the title compounds were performed as described previously.[23] The atomic composition of the precursors and the final compounds were determined by a Cameca SX-100 electron probe microanalyzer (EPMA) via a method developed by Donovan et al.[25]

X-ray reflectivity (XRR) and X-ray diffraction (XRD) were used to determine the total thickness and crystallinity of the films respectively. Both the XRR and XRD measurements were performed on a Bruker D8 AXS diffractometer equipped with a Cu K_α (0.154 nm) radiation source operated at 40 kV and 40 mA, a Göbel mirror, and Bragg–Brentano optics geometry. Locked coupled θ - 2θ scans were collected from (0–10°) and (6–65°) 2θ for XRR and XRD respectively. Rietveld refinements were performed using the FullProf program package.[26]

In-plane X-ray diffraction scans were partially collected at Beamline 33BM at the Advanced Photon Source at Argonne National Lab where the incident X-ray beam had a wavelength of 0.1236 nm and on a Rigaku Smartlab X-ray diffractometer with Cu K_α radiation (λ = 0.15418 nm). The in-plane lattice parameters were refined from a least squares fits to the position of the indexed Bragg-reflections.

Samples for high angle annular dark field scanning transmission electron microscopy (HAADF-STEM) were prepared using FEI Helios dual beam using methods developed by Schaffer et al.[27] HAADF-STEM images were acquired on an FEI Titan 80-300. The sample was aligned in the microscope along the nearest silicon substrate zone axis.

Temperature-dependent resistivity measurements were conducted via a standard van der Pauw technique. Indium contacts were made to the four corners of the cross arms. Sheet resistance is then determined by sourcing current through two of the cross arms with a programmable current source while stabilizing the temperature between 20-295 K. The potential across the remaining two cross arms was measured by a nanovoltmeter. Total resistivity of the films is then obtained from the product of the sheet resistance and the total thickness of the films. Hall measurements were conducted at a constant current value of 0.100 A. The Hall voltage was obtained from the slope of magnetic field (0-1.6 T) vs. voltage plot between 20 and 295 K.

Results and discussion

Synthesis and Structure

The method and calibration process of synthesizing the compounds is described in detail elsewhere.[23] Briefly, the precursors are designed through physical vapor deposition of the constituting elements (Sn, Nb and Se). A sequence that resembles the targeted compounds is evaporated onto a silicon substrate with the correct stoichiometric and thickness ratio of the final compounds. Stoichiometric ratios of 1:1, 1:2 and 1.16:1 for Sn:Se, Nb: Se and Sn: Nb were targeted respectively. For each sample ($([SnSe]_{1.16})_m(NbSe_2)_2$), m layers of SnSe (m = 1-20) and two layers of $NbSe_2$ were repeatedly deposited until a thickness of ~ 50 nm was reached. A slight excess amount of Se (4 -5%) was deposited to compensate for selenium vapor loss during the annealing process.

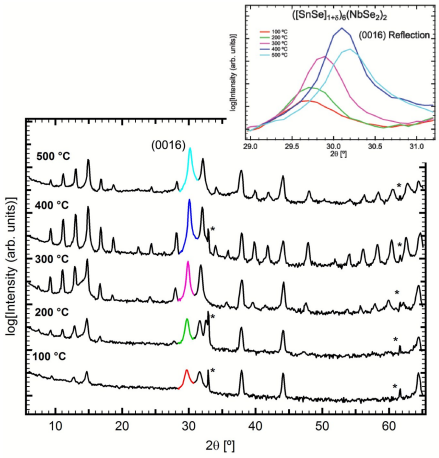

Figure 1. Annealing study of a (6,2) compound at different temperatures for 20 minutes. The 00*l* diffraction peaks are at a maximum intensity and narrowest FWHM at 400 °C. The inset

highlights the (0016) peak as a function of annealing temperature. (*) Mark Si-substrate peaks.

An annealing study was conducted to define the optimum annealing conditions the compounds form at. Five pieces of the same (6,2) sample were annealed at five different annealing temperatures for 20 minutes. Figure 1 displays the X-ray diffraction patterns of the five samples after annealing. With increasing temperature, more higher order peaks appear indicating the increasing crystallinity of the compounds. At 400 °C, the full width at half maximum (FWHM) becomes the narrowest and the intensity of the superlattice peaks maximum due to the optimal crystallographic alignment of the film perpendicular to the substrate. All 00*l* Bragg maxima can be indexed to the repeating unit thickness (*c*-lattice parameter). A shift of diffraction peaks to higher angles as a function of increasing temperature is observed due to loss of selenium vapor during annealing.

Table 1: *c*-lattice parameters and FWHM at 28° 2θ for $([SnSe]_{116})_m(NbSe_2)_2$

m [Number of SnSe Layers]	*c*-lattice Parameter [Å]	FWHM [°] at 28° 2θ
1	18.58(7)	0.260
2	24.37(6)	0.265
3	30.19(5)	0.230
4	35.94(6)	0.285
5	41.7(2)	0.300
6	47.46(9)	0.263
8	59.1(4)	0.286
10	70.6(5)	0.271
15	101(2)	0.281
20	129(1)	0.310

After defining the synthesis conditions, samples with SnSe layers ranging from (1-20) were synthesized using similar conditions. Figure 2 contains specular diffraction patterns of all the ten compounds showing the formation of the intended superlattice and high crystalline quality. The *c*-lattice parameters of SnSe and $NbSe_2$ were extracted from the slope and intercept of a linear fit for total *c*-lattice parameter vs *m* plot to be 0.579(3) nm and 1.281(4) nm respectively. The SnSe *c*-lattice parameter is within the range reported for SnSe containing misfit layer compounds and ferecrystals.[28] The thickness of the $NbSe_2$ is observed to be exactly double the thickness of a single $NbSe_2$ layer observed in the (*m*,1) compounds.[23]

In order to get a deeper insight into the structural changes in the double layer $NbSe_2$ versus the single layer $NbSe_2$, Rietveld refinements of both the (4,1) and the (4,2) compounds were carried out. The puckering in the (4,2) compound of the outer most SnSe layer is significantly larger than the (4,1) compound. Also the distance between the SnSe and the $NbSe_2$ is smaller in the (4,2) compound, suggesting a stronger interaction between layers. In both structures, the puckering of the inner layers of the SnSe unit decreases from the outer layer to the inner layer, with the inner most layer having the lowest puckering values. This is indicative of a smaller charge transfer contribution of the inner layers. This observation is consistent with an earlier report on SnSe in $([SnSe]_{1.15})_m(VSe_2)_1$.[28] In contrast to the (4,1) compound, the $NbSe_2$ in the (4,2) compound is not confined to be symmetrical, the results observed show lack of distortion and similar magnitude in the distances of Se-Nb-Se trilayer.

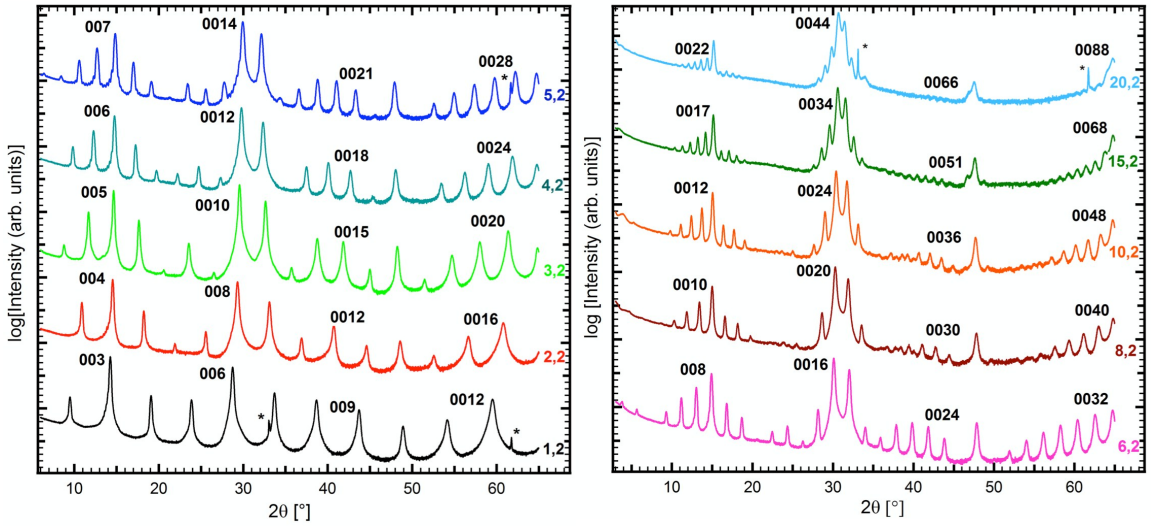

Figure 2: 00*l* diffraction patterns of $([SnSe]_{1+\delta})_m(NbSe_2)_2$ with each peak corresponding to the specific *c*-lattice parameter. Peaks designated by (*) correspond to silicon substrate peaks.

Table 2: In-plane lattice parameters of the SnSe and $NbSe_2$ constituents, and the resulting misfit parameter, δ, for $[(SnSe)_{1+\delta}]_m(NbSe_2)_2$

	(1,2)	**(2,2)**	**(3,2)**	**(6,2)**	**(10,2)**	**(20,2)**
a-lattice SnSe (Å)	0.4243(2)	0.4249(5)	0.4291(5)	0.4314(1)	0.4344(3)	0.4369(2)
b-lattice SnSe (Å)	0.4261(2)	0.4226(4)	0.4232(5)	0.4229(1)	0.4228(4)	0.4223(1)
a-lattice $NbSe_2$ (Å)	0.3459(2)	0.3463(1)	0.3466(2)	0.3457(1)	0.3465(5)	0.3467(1)
δ	0.146	0.146	0.146	0.135	0.132	0.128

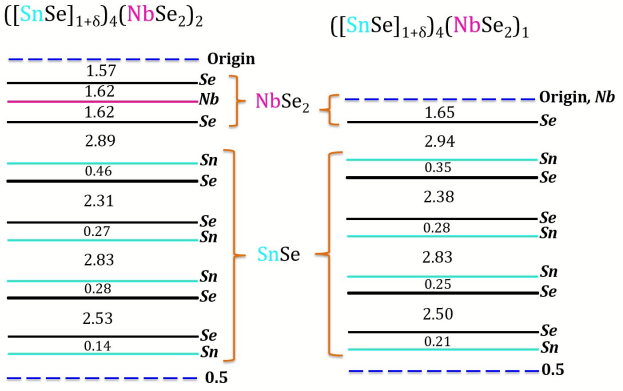

Figure 3. Atomic plane distances (in nm) along the c-axis from Rietveld refinements of $([SnSe]_{1+\delta})_4(NbSe_2)_2$ and $([SnSe]_{1+\delta})_4(NbSe_2)_1$ compounds. The structures were refined in the space group *P*-3*m*1which contains mirror planes (at origin and 0.5 indicated by blue dashed lines) perpendicular to the c-direction.

In-plane diffraction of selected compounds revealed the independent crystal lattices of the constituting units as typically observed for ferecrystals.[17] Similar to the (*m*,1) compounds, the SnSe reflections indicate the distortion of the basal unit from square to rectangle (Figure 4a) . At larger values of the SnSe, a higher degree of distortion is observed (Table 2 and Figure 4b). In comparison, the distortion of SnSe in (*m*,1) and (*m*,2) shows a similar trend and magnitude as a function of *m* indicating the lack of strain from the additional $NbSe_2$ layer. The $NbSe_2$ constituent in the (*m*,2) compounds generally show a slightly smaller *a*-lattice parameter resembling the a-lattice parameter of bulk 2*H*-$NbSe_2$ (0.345(1) nm) [29] rather than the 1*T*-$NbSe_2$ polytype (0.353(1) nm).[30]

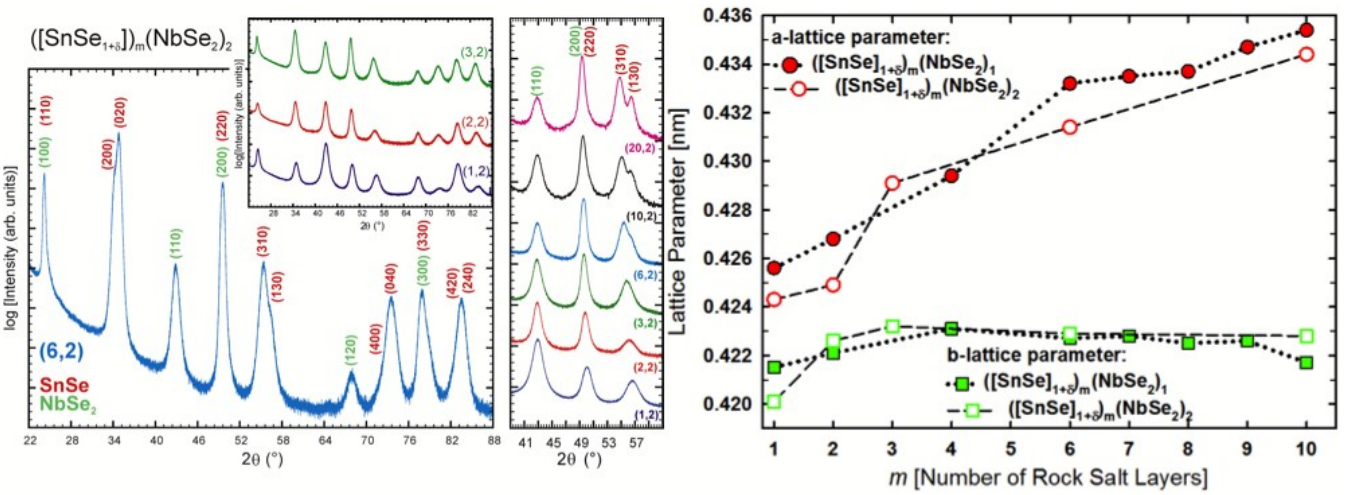

Figure 4: a) In-plane diffraction pattern of $([SnSe]_{1+\delta})_6(NbSe_2)_2$ with both SnSe and $NbSe_2$ independent lattice parameters indexed. The inset shows a stacked *hk*0 patterns of $([SnSe]_{1+\delta})_m(NbSe_2)_2$. B) *a*- and *b*-lattice dependence on *m* for both $([SnSe]_{1+\delta})_m(NbSe_2)_1$ and $([SnSe]_{1+\delta})_m(NbSe_2)_2$ compounds.

The HAADF-STEM image in Figure 5 shows the representative (6,2) compound, where a repeating sequence of six SnSe double layers and two trilayers of $NbSe_2$ is observed. In the part of the compound shown in Figure 5, several crystallographic orientations and two different coordination environments for the Nb in the $NbSe_2$ are observed. The crystal faces corresponding to the 1*T*- and 2*H*-$NbSe_2$ polytypes are highlighted. The change in coordination of the Nb from trigonal prismatic (2*H*-$NbSe_2$) to octahedral (1*T*-$NbSe_2$) was observed in the (*m*,1) compounds and in intercalated TMDs, which is evidence of charge transfer between the constituents.[31] The presence of rotational disorder between the different subunits is evident from the different crystal faces of SnSe and $NbSe_2$ observed in the image. This turbostratic disorder is a signature feature of ferecrystalline compounds is inherent to both *(m*,1) and (*m*,2) series of compounds.[31]

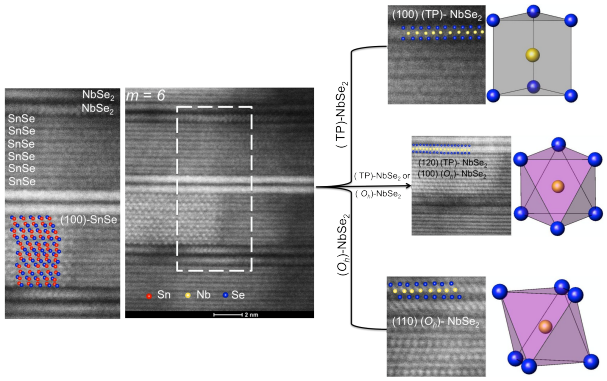

Figure 5. STEM image of $([SnSe]_{1+\delta})_6(NbSe_2)_2$ with both coordination of Nb in $NbSe_2$: octahedral and trigonal prismatic.

Electrical Properties

Figure 6a displays the electrical resistivity as a function of temperature between 50 and 300 K for compounds with *m* values of 1-6. All compounds exhibit metallic behavior within this temperature range. As seen in Figure 6b, increasing the number of SnSe layers to *m* = 8-10 results in a small upturn at lower temperatures indicating localization of carriers. Compounds with *m* values of 15 and 20, exhibit a significantly larger increase in the resistivity as the temperature is lowered.

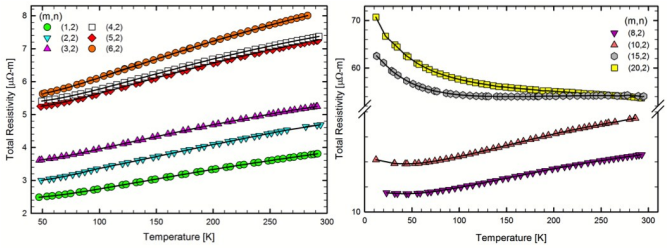

Figure 6. Temperature dependent electrical resistivity of $([SnSe]_{1+\delta})_m(NbSe_2)_2$.

The systematic increase of resistivity values with increasing *m* is caused by the decreasing carrier concentration, calculated from the Hall coefficient assuming a single band model as shown in Figure 7. The decline in carrier concentration is attributed to the increasing proportion of the sample which is semiconducting SnSe and also an increasing charge transfer from the SnSe to the $NbSe_2$ as a function of SnSe thickness. $NbSe_2$ has been reported to be a *p*-type metal where empty states dominate the conduction. When intercalated with SnSe, electrons are transferred into the d band of the Nb quenching

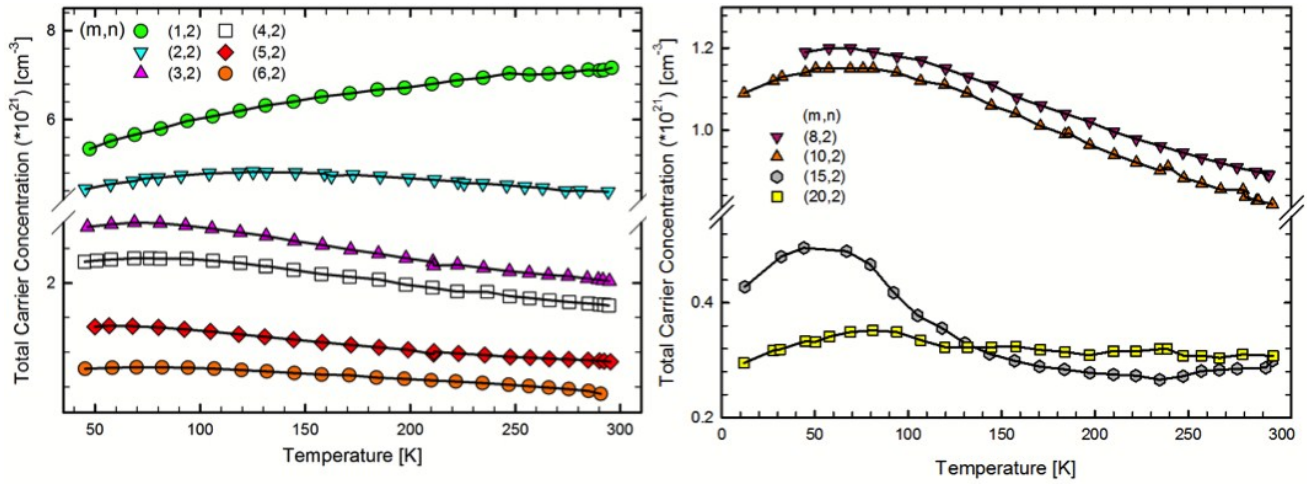

Figure 7. Temperature dependent carrier concentration of $([SnSe]_{1+\delta})_m(NbSe_2)_2$.

the empty states and leading to a more rapid decline in carrier concentration than what would be expected from the proportion of the semiconducting SnSe in the unit cell. For compounds with $m > 1$, the carrier concentration increases with lowering temperature. This uncommon behavior for semiconductors and/or metals can perhaps be a consequence of assuming a single band model. In general, the temperature dependence of the (m,2) compounds follow the same trend as that of the (m,1) compounds.

Mobility systematically increases with m showing a negative slope as a function of temperature for m values of 1 and 2. A relatively temperature independent mobility is observed for values of m = 3-10. A positive slope in the temperature dependence is observed for m = 15. In general, at lower m values the temperature dependence of the mobility is thought to be dominated by the carriers in $NbSe_2$. At higher m values, the carriers in the SnSe start to contribute causing a switch in the temperature dependence. Mobility values for the (5,2) and (6,2) compounds are higher than those found in single crystalline $NbSe_2$.[32]

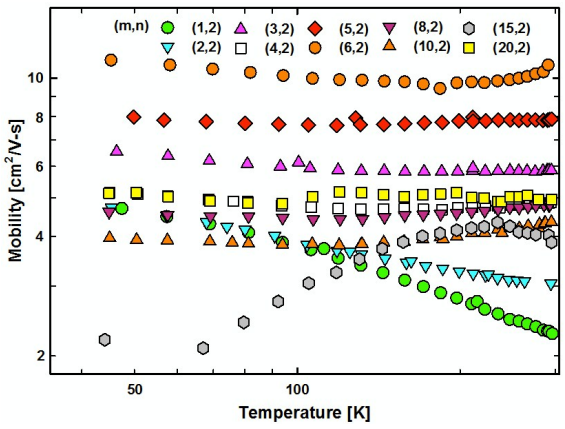

Figure 8. Temperature dependent mobility of $([SnSe]_{1+\delta})_m(NbSe_2)_2$.

In order to identify, if charge transfer or dimensionality have the greater effect on the transport properties, compounds in both series, (m,1) and (m,2), with the same m/n ratio are compared. They should exhibit the same electrical properties assuming similar charge transfer occurs. Conceptually, two units of the (1,1) compound can easily be converted into a (2,2) building block by rotating a (1,1) unit cell by 180° (see Figure 9). The significant differences between two compounds of similar m/n ratios are the additional SnSe-$NbSe_2$ interfaces present in the (m,1) compounds and the $NbSe_2$-$NbSe_2$ interface that is only present in the (m,2) compounds.

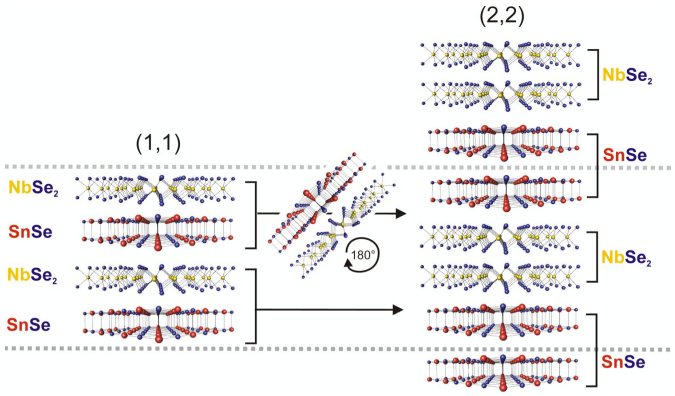

Figure 9. Schematic of same m/n ratios of $([SnSe]_{1+\delta})_1(NbSe_2)_1$ and $([SnSe]_{1+\delta})_2(NbSe_2)_2$ highlighting the similarity of both structures within the grey boundaries.

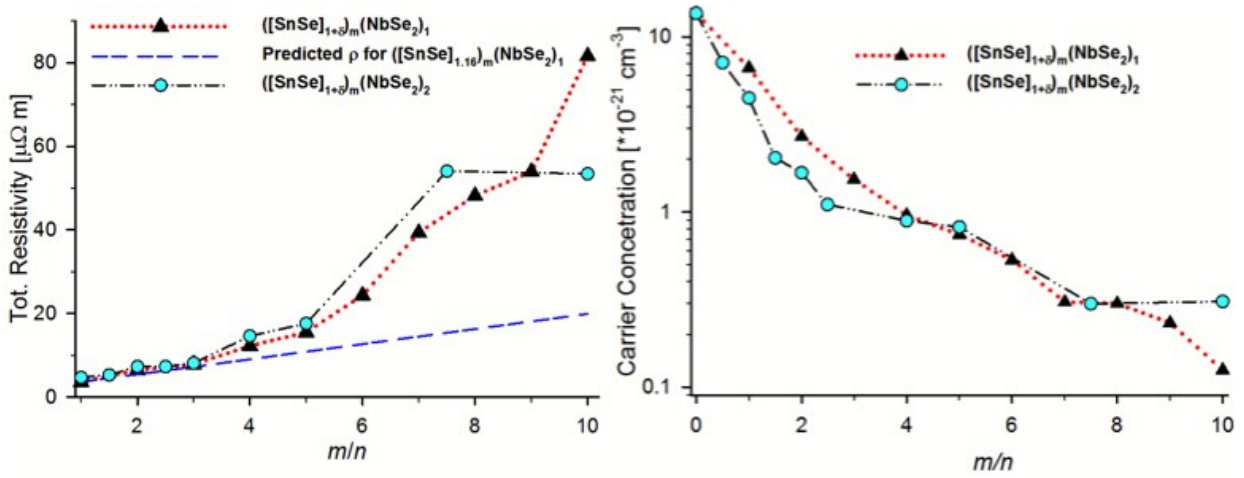

Figure 10. a) Total electrical resistivity and b) carrier concentration of $([SnSe]_{1+\delta})_m(NbSe_2)_1$ and $([SnSe]_{1+\delta})_m(NbSe_2)_2$ at room temperature as a function of *m*/*n* ratio.

As shown in Figure 10a, the electrical resistivities for both compounds show a similar change in magnitude when plotted as a function of the *m*/*n* ratio, indicating the difference in interfaces between (*m*,1) and (*m*,2) and, thus dimensionality, has only a minor influence. As shown in Figure 10b, the extent of charge transfer between the constituents is similar when plotted as a function of the *m*/*n* ratio. For the (20,2) compound, the extent of charge transfer is less than expected, suggesting that we have reached the thickness limitation of charge transfer. Comparing room temperature mobility values for the (*m*,2) and (*m*,1) compounds with the same *m*/*n* ratio shows that the difference in interfaces in general has no influence (Figure 11). The unusually high mobility values for the (5,2) and (6,2) compounds were unexpected. For the *(m*,1) series of compounds the (7,1) compound was also found to have an anomalously large mobility value. All of these mobility values are higher than found in bulk single crystals of $NbSe_2$. While it may be a coincidence, it is interesting that these higher mobility values occur for similar thicknesses of SnSe, perhaps suggesting that the *b*-axis lattice parameters for these *m* values result in an interfacial structure that produces less carrier scattering.

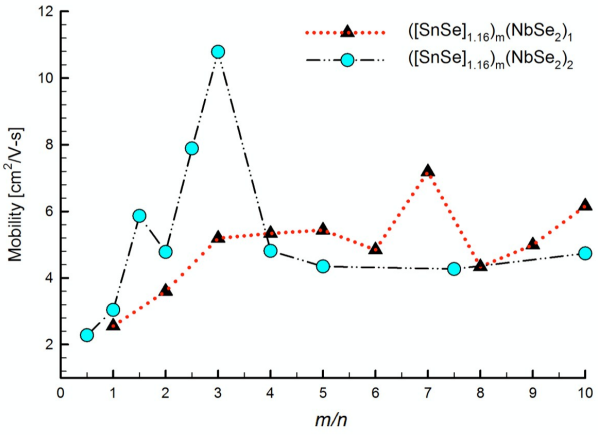

Figure 11. Mobility of $([SnSe]_{1+\delta})_m(NbSe_2)_1$ and $([SnSe]_{1+\delta})_m(NbSe_2)_2$ at room temperature as a function of *m*/*n* ratio.

Conclusions

The compounds $([SnSe]_{1+\delta})_m(NbSe_2)_2$, where $1 \leq m \leq 20$, were synthesized by systematically changing the SnSe layer thickness. A systematic change of 0.579(3) nm in the *c*-lattice parameter as a function of *m* was observed. The thickness of the double $NbSe_2$ layer was determined to be 1.281(4) nm corresponding to twice the value of a single $NbSe_2$ layer. Structurally, this series of compounds is similar to $([SnSe]_{1+\delta})_m(NbSe_2)_1$ with an almost identical distortion of the in-plane lattice parameters of the SnSe layer as a function of *m*. However, Rietveld refinements of a (4,2) and a (4,1) compound revealed a larger puckering between the Sn and Se planes in the rocksalt layer and a smaller distance between the SnSe-$NbSe_2$ layers in the (4,2) compound. We observed two different coordination environments of the Nb atom: trigonal prismatic and octahedral, and evidence for extensive turbostratic disorder between subsequent constituent layers in HAADF-STEM images. For compounds with $m \leq 10$, a metallic temperature dependence of resistivity is observed. Compounds with *m*

values of 15 and 20 have increases in resistivity at low temperatures, suggesting carrier localization. The electrical resistivities of both series of compounds, (*m*,1) and (*m*,2), scaled by the *m*/*n* ratio have a similar magnitude and temperature dependence indicating the difference in interfaces between the two series of compounds has a minor influence. The carrier concentrations for the two series also have similar behaviors as a function of the *m*/*n* ratio, suggesting comparable amounts of charge transfer occur between the constituents. In conclusion, although the effect of dimensionality can't be ignored, the dominant effect on the transport properties of $([SnSe]_{1+\delta})_m(NbSe_2)_1$ and $([SnSe]_{1+\delta})_m(NbSe_2)_2$ ferecrystals arises from charge transfer.

Acknowledgements

The authors thank Josh Razink and Robert Fischer in CAMCOR for assistance in preparing TEM samples and collecting STEM images. Grant MRI 0923577 provided funding for the dual beam FIB used to make TEM cross sections. The authors acknowledge support from the National Science Foundation under grant DMR-1266217. Coauthor MF acknowledges support from the National Science Foundation through CCI grant number CHE-1102637. The authors thank Jenia Karapetrova for assistance at Beamline 33-C at the Advanced Photon Source (APS) in Argonne National Laboratories. The use of the APS was supported by the U.S. Department of Energy, Office of Science, and the Office of Basic Energy Sciences, under Contract No. DE-AC02-06CH11357.

Notes and references

[a] Department of Chemistry and Materials Science Institute, 1253 University of Oregon, Eugene, Oregon 97403, United States.

Electronic Supplementary Information (ESI) available: detailed results of the Rietveld refinement including a table of parameters and the refinements patterns are available. See DOI: 10.1039/b000000x/

1 K. S. Novoselov, a K. Geim, S. V Morozov, D. Jiang, Y. Zhang, S. V Dubonos, I. V Grigorieva and a a Firsov, *Science*, 2004, **306**, 666–9.
2 B. Radisavljevic, a Radenovic, J. Brivio, V. Giacometti and a Kis, *Nat. Nanotechnol.*, 2011, **6**, 147–50.
3 G. Tang, J. Zhang, C. Liu, H. Tang and C. Li, *Mater. Lett.*, 2014, **124**, 289–292.
4 Y. H. Huang, C. C. Peng, R. S. Chen, Y. S. Huang and C. H. Ho, *Appl. Phys. Lett.*, 2014, **105**, 093106.
5 N. Staley, J. Wu, P. Eklund, Y. Liu, L. Li and Z. Xu, *Phys. Rev. B*, 2009, **80**, 184505.
6 P. Sekar, E. C. Greyson, J. E. Barton and T. W. Odom, *J. Am. Chem. Soc.*, 2005, **127**, 2054–5.
7 Y. Shi, H. Li and L.-J. Li, *Chem. Soc. Rev.*, 2014.
8 H. . Wang, H. . Feng and J. . Li, *Small*, 2014, **10**, 2165–2181.
9 C. Tan and H. Zhang, *Chem. Soc. Rev.*, 2014.
10 L. Yang, X. Cui, J. Zhang, K. Wang, M. Shen, S. Zeng, S. a Dayeh, L. Feng and B. Xiang, *Sci. Rep.*, 2014, **4**, 5649.
11 A. Splendiani, L. Sun, Y. Zhang, T. Li, J. Kim, C.-Y. Chim, G. Galli and F. Wang, *Nano Lett.*, 2010, **10**, 1271–5.
12 M. Chhowalla, H. S. Shin, G. Eda, L.J. Li, K. P. Loh and H. Zhang, *Nat. Chem.*, 2013, **5**, 263–75.
13 Y. Li, S. Tongay, Q. Yue, J. Kang, J. Wu and J. Li, *J. Appl. Phys.*, 2013, **114**, 174307.
14 K. Novoselov and D. Jiang, *Proc. Natl. Acad. Sci.*, 2005, **102**, 10451–10453.
15 M. Falmbigl, A. Fiedler, R. E. Atkins, S. F. Fischer and D. C. Johnson, *Nano Lett.*, *Accepted*. 2014.
16 D. Waldmann, J. Jobst, F. Speck and T. Seyller, *Nat. Mater.*, 2011, **10**, 357–360.
17 M. Beekman, C. L. Heideman and D. C. Johnson, *Semicond. Sci. Technol.*, 2014, **29**, 064012.
18 D. B. Moore, M. Beekman, S. Disch and D. C. Johnson, *Angew. Chem. Int. Ed. Engl.*, 2014, **53**, 5672–5.
19 M. Beekman, G. Cogburn, C. Heideman, S. Rouvimov, P. Zschack, W. Neumann and D. C. Johnson, *J. Electron. Mater.*, 2012, **41**, 1476–1480.
20 C. Heideman, S. Tepfer and Q. Lin, *J. Am. Chem. Soc.,* 2013*,* **135**, 11055-11062 .
21 M. M. Smeller, C. L. Heideman, Q. Lin, M. Beekman, M. D. Anderson, P. Zschack, I. M. Anderson and D. C. Johnson, *Zeitschrift für Anorg. und Allg. Chemie*, 2012, **638**, 2632–2639.
22 M. B. Alemayehu, G. Mitchson, B. E. Hanken, M. Asta and D. C. Johnson, *Chem. Mater.*, 2014, **26**, 1859–1866.
23 M. B. Alemayehu, M. Falmbigl, K. Ta, C. Grosse, R. D. Westover, S. R. Bauers, S. F. Fischer and D. C. Johnson, *Chem. Mater.*,*Submitted*. 2014.
24 L. Fister, X. M. Li, J. McConnell, T. Novet and D. C. Johnson, *J. Sci. Vac. Technol.*, 1993, **11**, 3014–3019.
25 T. M. Phung, J. M. Jensen, D. C. Johnson, J. J. Donovan and B. G. Mcburnett, *X-Ray Spectrom.*, 2008, **37**, 608–614.
26 T. Roisnel.; J. Rodriguez-Carvajal, *Anal. Mater. Sci. Forum*, 2001, **118**, 378–381.
27 S. Schaffer, B. Schaffer and Q. Ramasse, *Ultramicroscopy*, 2012, **114**, 62–71.
28 R. Atkins, S. Disch, Z. Jones, I. Haeusler, C. Grosse, S. F. Fischer, W. Neumann, P. Zschack and D. C. Johnson, *J. Solid State Chem.*, 2013, **202**, 128–133.
29 B. E. Brown and D. J. Beerntsen, *Acta Crystallogr.*, 1965, **18**, 31–36.
30 F. Kadijk, *J. Less Common Met.*, 1971, **23**, 437–441.
31 R. Mas-Ballesté, C. Gómez-Navarro, J. Gómez-Herrero and F. Zamora, *Nanoscale*, 2011, **3**, 20–30.
32 H. N. S. Lee, *J. Appl. Phys.*, 1969, **40**, 602.

